PCCP

PAPER

View Article Online
View Journal | View Issue

Cite this: *Phys. Chem. Chem. Phys.*, 2017, **19**, 19683

Time-resolved photoelectron spectroscopy of IR-driven electron dynamics in a charge transfer model system

Mirjam Falge,†[a] Friedrich Georg Fröbel,†[b] Volker Engel *[a] and Stefanie Gräfe *[b]

Received 22nd March 2017,
Accepted 26th April 2017

DOI: 10.1039/c7cp01832k

rsc.li/pccp

If the adiabatic approximation is valid, electrons smoothly adapt to molecular geometry changes. In contrast, as a characteristic of diabatic dynamics, the electron density does not follow the nuclear motion. Recently, we have shown that the asymmetry in time-resolved photoelectron spectra serves as a tool to distinguish between these dynamics [Falge *et al.*, *J. Phys. Chem. Lett.*, 2012, **3**, 2617]. Here, we investigate the influence of an additional, moderately intense infrared (IR) laser field, as often applied in attosecond time-resolved experiments, on such asymmetries. This is done using a simple model for coupled electronic-nuclear motion. We calculate time-resolved photoelectron spectra and their asymmetries and demonstrate that the spectra directly map the bound electron–nuclear dynamics. From the asymmetries, we can trace the IR field-induced population transfer and both the field-driven and intrinsic (non-)adiabatic dynamics. This holds true when considering superposition states accompanied by electronic coherences. The latter are observable in the asymmetries for sufficiently short XUV pulses to coherently probe the coupled states. It is thus documented that the asymmetry is a measure for phases in bound electron wave packets and non-adiabatic dynamics.

1 Introduction

Electronic dynamics can be investigated by time-resolved measurements with ultra-short laser pulses. As electronic dynamics normally take place on the attosecond time-scale, the time-resolution of the experiment has to reach this order of magnitude.[1] Pump–probe ionization set-ups are one way to achieve this, as it is possible to detect transient ions and photoelectron signals resolved in time, kinetic energy and angular distribution. Most attosecond pump–probe experiments employ XUV + NIR excitation schemes where the relative position of the ultra-short XUV pulse to the optical cycle of a longer NIR pulse serves as a time ruler for the attosecond resolution of the detected signals.[2–5] In such experiments, the NIR laser pulse often rather creates the electronic dynamics[6–8] than facilitating the observation of the intrinsic dynamics of the system.

With regard to molecules, the motion of electrons usually is highly correlated to the dynamics of the nuclei due to the strong Coulomb-interactions between the charged particles. Concerning this motion, two opposite situations can be characterized.[9] When the dynamics proceeds adiabatically, electrons follow the nuclear motion. That is, upon geometry changes, the electronic density adapts to the variation of the nuclear positions. On the other hand, for a diabatic motion, the electron density merely stays constant so that a varying molecular structure does not, or only weakly, influences the electron dynamics. The latter case is usually accompanied by non-adiabatic transitions which are characterized by strong non-adiabatic couplings between the nuclear and electronic degrees of freedom.

Referring to the two dynamical cases described, one might ask if it is possible to experimentally differentiate between them. In a former work, we addressed this question with regard to asymmetries in time-resolved photoelectron spectra.[10] Such asymmetries were studied extensively in the last few years, both experimentally[11–17] and theoretically.[18–22] From a theoretical point of view, it is extremely difficult to quantum mechanically describe the correlated dynamics of electrons and nuclei when solving the time-dependent Schrödinger equation for the coupled motion. This can only be done for systems consisting of a few particles and in reduced dimensions. To gain insight into the basic physics of coupled electron–nuclear motion in external fields it is of advantage to set up reasonable models. One such model is that of a single electron and a single nucleus moving in one dimension between two additional fixed nuclei (Shin–Metiu model).[23,24] The proposed approach allows, when adopting different parameterizations for particle interactions, switching between the cases of adiabatic and diabatic charge

[a] *Institute for Physical and Theoretical Chemistry, Julius Maximilians Universität Würzburg, Germany. E-mail: voen@phys-chemie.uni-jena.de*
[b] *Institute for Physical Chemistry and Abbe Center for Photonics, Friedrich-Schiller-Universität Jena, Germany. E-mail: s.graefe@uni-jena.de*
† These authors contributed equally to this work.

transfer dynamics. The original model and its variations have been employed to mimic various dynamics and simulate spectroscopic observables.[10,25–34]

Ionizing a one-dimensional system provides the simplest case of a PAD (photoelectron angular distribution) as there are only two possible directions for the emission of photoelectrons. In the present paper, we extend our former work on time-resolved photoelectron spectroscopy in the Shin–Metiu model[10,29] and investigate a possibility to enhance weak photoelectron signals stemming from the intrinsic dynamics by the interaction with a phase-modulated IR pulse which precedes an XUV pulse. In particular, we address the sensitivity of these signals to coupled adiabatic and diabatic electron–nuclear motion and the initial momentum distribution of the nuclear–electron wave packet.

The paper is organized as follows: in Section 2, we describe the Shin–Metiu model and the computation of photoelectron asymmetries. Numerical results are presented in Section 3 and Section 4 provides a summary and conclusion.

2 Theoretical background

2.1 Charge-transfer model

We apply a model originally introduced by Shin and Metiu[23,24] to describe non-adiabatic effects in charge transfer dynamics. Here, a single active electron and a nucleus move along the coordinates x and R, respectively, and interact with two ions at fixed internuclear distances $\pm L/2$. The potential energy of the system is parameterized by screened Coulomb interactions between the electron and the nuclei (expressed *via* the error functions, erfs), and bare Coulomb repulsion terms for the nuclei (atomic units are used unless stated otherwise):

$$V(x,R) = \frac{Z^2}{|L/2-R|} + \frac{Z^2}{|L/2+R|} - \frac{Z\,\mathrm{erf}(|L/2-x|/R_\mathrm{f})}{|L/2-x|} - \frac{Z\,\mathrm{erf}(|L/2+x|/R_\mathrm{f})}{|L/2+x|} - \frac{Z\,\mathrm{erf}(|R-x|/R_\mathrm{c})}{|R-x|}. \quad (1)$$

Here, we set the nuclear charges to $Z = 1$ for all nuclei and choose a screening parameter of $R_\mathrm{f} = 1.5$ Å. The distance between the fixed ions is $L = 10$ Å, and the origin of the coordinate system is defined to be at the midpoint between the fixed ions. The value of the screening parameter R_c plays a particular role, as its value allows the characterization of the systems dynamics, ranging from adiabatic to completely diabatic motion, see below. The dynamics of the system follows the time-dependent Schrödinger equation, which reads as:

$$i\frac{\partial}{\partial t}\psi(x,R,t) = \left[-\frac{1}{2M}\frac{\partial^2}{\partial R^2} - \frac{1}{2}\frac{\partial^2}{\partial x^2} + V(x,R) + W(x,R,t)\right]\psi(x,R,t) = [T_R + T_x + V(x,R) + W(x,R,t)]\psi(x,R,t). \quad (2)$$

Here, M is chosen as the proton mass and $W(x,R,t)$ is the dipole interaction with the external field $E(t)$ in length gauge:

$$W(x,R,t) = (x - R)\,E(t). \quad (3)$$

The electric field contains the combined interaction of a moderately intense, few-cycle infrared (IR) electric field (E_IR) and an ionizing ultrashort XUV-field (E_XUV):

$$E_\mathrm{IR}(t) = E_{0,\mathrm{IR}} f_\mathrm{IR}(t - T_\mathrm{IR})\cos[\omega_\mathrm{IR}(t - T_\mathrm{IR}) + \phi_\mathrm{IR}], \quad (4)$$

$$E_\mathrm{XUV}(t) = E_{0,\mathrm{XUV}} f_\mathrm{XUV}(t - T)\cos[\omega_\mathrm{XUV}(t - T)]. \quad (5)$$

In the above equation, $E_{0,i}$ is the field strength, $f_i(t - T_i)$ the (Gaussian) pulse envelope function centered at time T_i, ω_i the frequency, and ϕ_IR the carrier-envelope phase (CEP).

For analysis, we numerically solve the electronic Schrödinger eigenvalue equation

$$[T_x + V(x,R)]\varphi_n(x;R) = V_n(R)\varphi_n(x;R), \quad (6)$$

providing the electronic (adiabatic) eigenfunctions $\varphi_n(x;R)$ and the eigenenergies $V_n(R)$, which are displayed in Fig. 1 as potential energy curves.

2.2 Numerical details

The time-dependent Schrödinger equation (eqn (2)) is numerically integrated on a grid in the range $[-240:240]$ Å with 1024 points in the x-direction and $[-6:6]$ Å with 256 points in the R-direction, using the split-operator technique[35] and the FFTW 3 library.[36] The time-step is set to 0.001 fs. The electronic eigenfunctions $\varphi_n(x,y)$ and eigenenergies $V_n(R)$ are obtained *via* imaginary time-propagation.[37]

To avoid grid reflections and to calculate photoelectron spectra, we divide the electronic grid into an inner and an outer, asymptotic region. In the latter, we neglect all Coulomb interactions so that the electron moves exclusively under the influence of the laser fields. The propagation then is carried out in momentum space using the velocity gauge for the

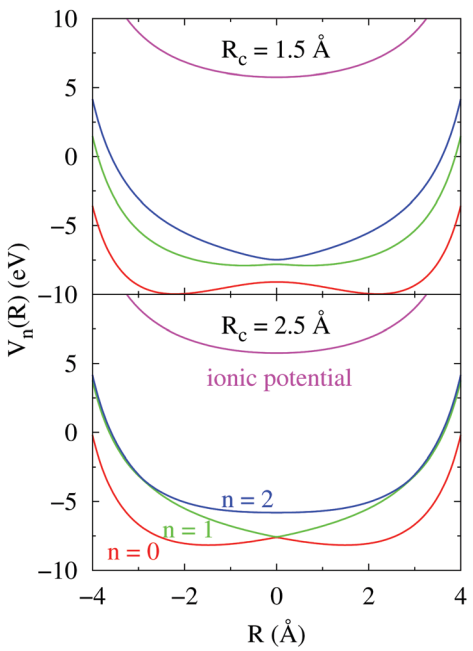

Fig. 1 Potential energy curves $V_n(R)$ and ionic potential curve for the adiabatic (R_c = 1.5 Å) and diabatic (R_c = 2.5 Å) cases, as indicated.

dipole interaction. The electron is thus solely propagated in momentum space. We split the total wave function by multiplication with a mask function,[38,39]

$$c(x,R) = [1 + e^{(|x|-x_{max}/1.3)/\beta}]^{-1}[1 + e^{40(|R|-R_{max}/1.3)/\beta}]^{-1}, \quad (7)$$

with the smoothing parameter β = 6 a.u., x_{max} = 240 Å and R_{max} = 6 Å. At each time step, we obtain an inner and an outer wave function as

$$\psi_{in}(x,R,t) = c(x,R)\ \psi(x,R,t),$$
$$\psi_{out}(x,R,t) = [1 - c(x,R)]\ \psi(x,R,t). \quad (8)$$

The outer part of the wave function is Fourier-transformed with respect to the electronic coordinate x into momentum space and coherently added to the parts already localized in the outer region. For long times, we obtain the wave function $\psi_{out}(p_x,R,T,t \to \infty)$ prepared by interaction with the XUV-pulse at time T. The photoelectron spectrum is then calculated as

$$\sigma(p_x, T) = \int |\psi_{out}(p_x, R, T, t \to \infty)|^2 dR. \quad (9)$$

The time-limit is defined as the time when the norm of the wave function in the inner (or outer) region becomes constant. Besides the photoelectron spectra, we also calculate the momentum resolved asymmetry

$$A(p_x, T) = \frac{\sigma^+(p_x, T) - \sigma^-(p_x, T)}{\sigma^+(p_x, T) + \sigma^-(p_x, T)}, \quad (10)$$

and the integrated asymmetry

$$A(T) = \frac{\sigma^+(T) - \sigma^-(T)}{\sigma^+(T) + \sigma^-(T)}. \quad (11)$$

The spectra $\sigma^{\pm}$ result from electrons emitted with positive (+) and negative (−) momenta, respectively.

3 Results

Similar to our former work, where we have characterized the limiting cases of adiabatic and diabatic dynamics *via* the asymmetry of the time-resolved photoelectron spectra,[10] we start with a vibrational wave packet in the electronic ground state and shortly recapitulate the basic features of the field-free dynamics. As stated above, the two different dynamics, adiabatic and diabatic, can be realized in this model system by choosing the value R_c correspondingly. For R_c = 1.5 Å, merely adiabatic dynamics proceeds, which means that most of the wave packet remains in the electronic ground state. Thus, within the picture suggested by the potential curves displayed in Fig. 1, the vibrational motion takes place in the ground state potential. Choosing a value of R_c = 2.5 Å results in an almost pure diabatic dynamics. This means that, starting in the ground state, the population is nearly completely transferred into the first excited state upon passing the symmetric configuration at R = 0, see Fig. 1.

3.1 Adiabatic dynamics

In the adiabatic case (R_c = 1.5 Å), we initiate vibrational dynamics by placing a vibrational wave packet centered around R_0 = −0.9 Å (with a width of β_R = 7.14 Å^{-2}) in the electronic ground state (n = 0),

$$\psi(x,R,t = 0) = N_0 e^{-\beta_R(R-R_0)^2} \varphi_0(x;R). \quad (12)$$

Without the external IR field, the dynamics is restricted to the ground state potential energy curve, with the electron adapting to the nuclear dynamics. The asymmetry in the photoelectron spectra which, for the case of no interacting IR field, is denoted as $A_0(T)$ in what follows, is calculated for a pulse with λ_{XUV} = 60 nm (20.7 eV) and 2.3 fs full width at half maximum (FWHM). Fig. 2 reflects these dynamics. Within a classical, intuitive picture, upon ionization, the electron retains its mean momentum and is emitted preferentially in the corresponding direction, thus leading to a time-dependent asymmetry in the photoelectron distribution. Note that within the Born–Oppenheimer (BO) form of the wave function, the expectation value of the electronic momentum is identically zero. This is because the ansatz neglects the time-dependence of the electronic wave function which, as the nucleus moves, follows the motion.

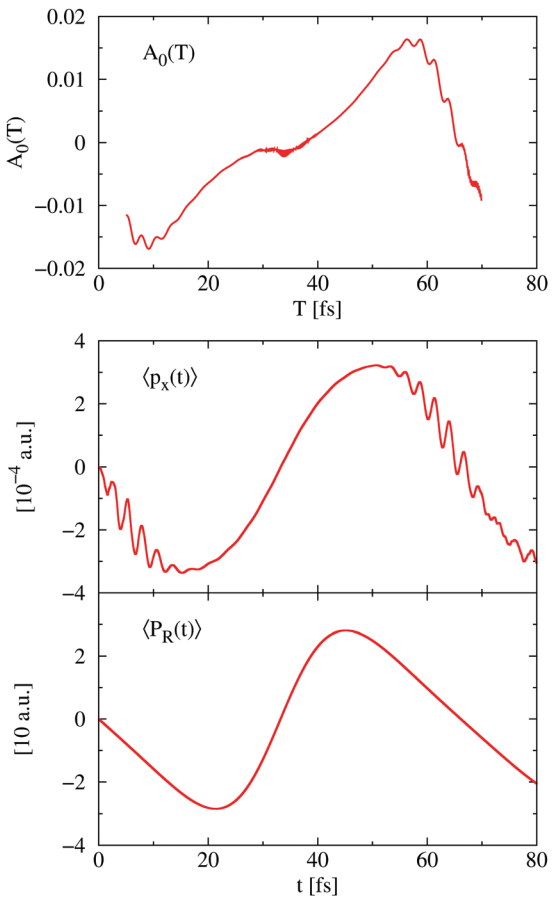

Fig. 2 Adiabatic dynamics. Upper panel: Time-resolved (integrated) asymmetry $A(T)$ probed with a λ_{XUV} = 60 nm (20.7 eV), 2.3 fs (FWHM) XUV pulse. Middle and lower panels: Expectation values of the electron ($\langle p_x(t)\rangle$) and nuclear ($\langle P_R(t)\rangle$) momenta, as indicated.

We now apply an additional moderately intense IR laser field with λ_{IR} = 1200 nm, FWHM = 14.7 fs, T_{IR} = 24 fs and $E_{0,IR}$ = 1×10^{11} W cm^{-2}. The IR field drives bound electron dynamics, and the electron momentum follows the dynamics imprinted by the vector potential of the IR field, see Fig. 3, upper panel. The more intense the field, the larger the momentum that can be acquired by the electron. Analogously to the (IR) field-free case, upon ionization with the XUV pulse, the electron retains its mean momentum and is emitted preferentially in the corresponding direction, thus leading to an asymmetry in the photoelectron distribution, as can be seen in Fig. 3, middle panel. As expected, for more intense fields (and correspondingly larger electron momenta), larger absolute values of the asymmetry $A(T)$ are obtained.

We note that, as the electron dynamics is driven by the field, the electron momentum ($\langle p_x(t)\rangle$) and, thus, the asymmetry $A(T)$ depend on the carrier–envelope phase ϕ_{IR} of the driving IR field. Let us compare the two cases, ϕ_{IR} = 0 and ϕ_{IR} = π, corresponding to (cosine) and -(cosine) pulses, respectively. The respective asymmetries are shown in the lower panel of Fig. 3. They cross at times, when the vector potential of the IR field is zero. At these times, the asymmetries display exactly the same value as in the field-free case. This indicates that the intrinsic dynamics remains unmodified and is still observable in the presence of a moderately intense laser field. To verify this assumption, we consider the sum of the asymmetries extracted from the pump–probe arrangements with CEP phases ϕ_{IR} as:

$$\begin{aligned} S(T) &= A(T,\phi_{IR} = 0) + A(T,\phi_{IR} = \pi) \\ &= A_0(T) + A_{IR}(T,\phi_{IR} = 0) \\ &\quad + A_0(T) + A_{IR}(T,\phi_{IR} = \pi). \end{aligned} \tag{13}$$

Here, we have decomposed the signal into contributions which stem from the IR-field free case (A_0) and from the additional asymmetry induced by the field (A_{IR}). If the IR field is not too intense, the sum $S(T)$ assumes a value two times that of the asymmetry $A_0(T)$ at times when a crossing of the curves for the two CEPs takes place. For more intense pulses, the field induces population transfer to higher lying electronic states thereby altering the systems dynamics. Then, $S(T)$ is no longer correlated with the field-free values, see Fig. 4. The curves in the figure document that for the two lowest field intensities, the signal $S(T)$ tracks twice the asymmetry $A_0(T)$. On the other hand, for an intensity of $I = 4 \times 10^{11}$ W cm^{-2}, substantial deviations are obtained. We have thus demonstrated that the bound electron dynamics induced by an IR field can be monitored *via* the asymmetry of the integrated photoelectron spectra. The sum of asymmetries induced by IR fields thereby is a direct measure of the intrinsic dynamics, as long as the field induced population transfer is negligible.

The photoelectron spectra and the momentum (energy)-resolved asymmetries $A(E = p_x^2/2,T)$ provide additional information on the systems dynamics. An example is shown in Fig. 5. Here, we employ: λ_{IR} = 1200 nm, FWHM = 14.7 fs, T_{IR} = 24 fs and $E_{0,IR}$ = 1×10^{11} W cm^{-2}. The photoelectron spectra $\sigma^{\pm}(E,T)$ show the characteristic streaking features, namely shifts in the energy as determined by the vector potential of the driving IR field at the ionization time.[2–4] Rich structures in the asymmetries can be seen: at small ionization times T < 10 fs, prior to the interaction with the IR pulse, electrons with higher kinetic energies

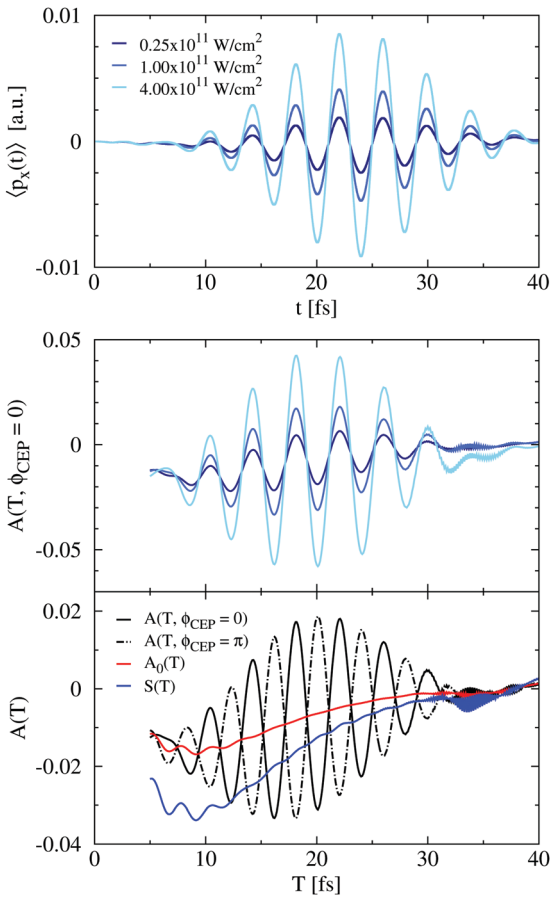

Fig. 3 Adiabatic dynamics. Upper panel: Expectation value of the electron momentum ($\langle p_x(t)\rangle$) driven by IR fields with different intensities, as labeled. Middle panel: Corresponding time-resolved asymmetries $A(T)$ of the system. The lower panel displays the results of two simulations, where the CEPs differ by a value of π, ϕ_{IR} = 0, π. For comparison, the asymmetry in the absence of an IR field is also included.

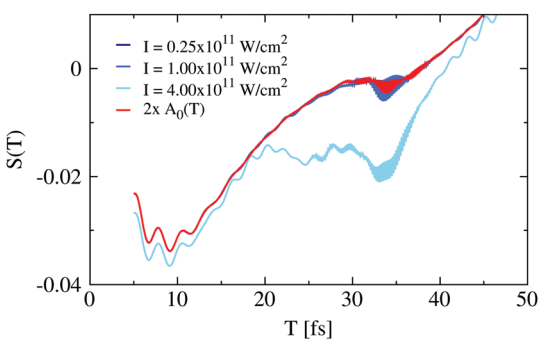

Fig. 4 Adiabatic dynamics: the sum $S(T)$ of the time-resolved asymmetries (eqn (13)) of the system interacting with an IR field is shown at different intensities, as labeled. For comparison, twice the asymmetry in the absence of an IR field ($A_0(T)$) is displayed.

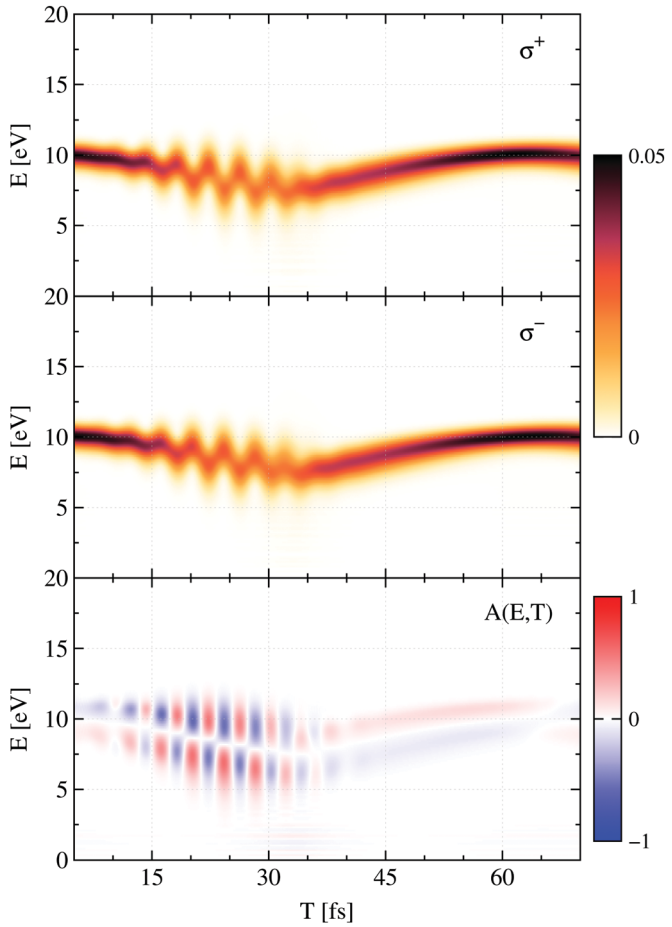

Fig. 5 Adiabatic dynamics: Time-resolved photoelectron spectra $\sigma^{\pm}(E,T)$ and asymmetries $A(E,T)$ of the system interacting with an IR field.

($E > 10$ eV) are preferentially emitted to the left (negative momenta), while electrons with smaller kinetic energies ($E < 10$ eV) are preferentially emitted to the right (positive momenta). The situation is reversed at larger ionization times $T > 45$ fs, after the IR pulse is switched off. During the interaction with the IR field, fast oscillations of the spectrally-resolved asymmetry can be seen with the oscillation period corresponding to the laser frequency.

At times, when an electron is driven to the left (acquiring negative momenta), the liberated electron flying to the left will receive an additional kick (shift) to the left, thus ending up at higher kinetic energies $\sigma^{-}(E,T)$. This can be clearly seen, *e.g.* around $t = 20$ fs. In contrast, a liberated electron ejected to the right is decelerated as the vector potential points into the opposite direction. Thus, the spectrum $\sigma^{+}(E,T)$ is shifted to lower kinetic energies. Consequently, at higher kinetic energies the asymmetry $A(E,T)$ assumes large negative values, while at lower kinetic energies the asymmetry assumes large positive values.

3.2 Non-adiabatic dynamics

We next investigate the non-adiabatic case, $R_c = 2.5$ Å and initiate the dynamics by positioning a vibrational wave packet around $R_0 = -3.0$ Å. Then, almost pure diabatic dynamics proceeds with population inversion after about 30 fs. Unlike the adiabatic case, the mean electronic momentum is not in phase with that of the nucleus as can be seen in Fig. 6 which also displays the asymmetry $A_0(T)$ (upper panel). During the non-adiabatic transition, $\langle p_x \rangle$ is small and positive, however, the normalized asymmetry $A_0(T)$ assumes relatively large negative values due to the interference of contributions to the ionization from the electronic ground and the first excited state, see ref. 10 for details.

Similar to the adiabatic case, we apply CEP-dependent IR fields ($\phi_{IR} = 0$) centered around $T_{IR} = 24$ fs – the time when the non-adiabatic transition occurs – and calculate the sum $S(T)$ of the asymmetries in the photoelectron spectra. As before, the intrinsic dynamics remains observable, as long as the field strength of the IR field is not too high which can be seen in the lower panel of Fig. 6.

3.3 Superposition states

In Sections 3.1 and 3.2, we considered the situations where the dynamics is mainly restricted to a single adiabatic state and a nearly complete non-adiabatic transition takes place, respectively. It is interesting to consider the case where already the initial wave packet has components in two electronic states. This is realized for the parameterization with $R_c = 1.5$ Å and initial wave packet superpositions as:

$$\psi_{\pm}(x,R,t=0) = N_0 e^{-\beta_R (R-R_0)^2} [\varphi_0(x;R) \pm \varphi_1(x;R)], \quad (14)$$

where $\pm$ denotes the positive or negative superposition, respectively. The initial (normalized) wave packet is centered around $R_0 = -2.5$ Å and has a (Gaussian) width of $\beta_R = 7.14$ Å^{-2}. As can be seen in Fig. 7 at shorter times, very fast oscillations of $\langle p_x(t) \rangle$ (and $\langle P_R(t) \rangle$) occur with a period of about 1.2 fs. The latter time corresponds to an energy difference of $\Delta E = V_1(R = -2.5\ \text{Å}) - V_0(R = -2.5\ \text{Å}) = 3.4$ eV and increases slightly as a function of time as the wave packet moves towards larger nuclear distances. This suggests that the oscillations are due to electronic coherences between the ground and first excited states. As the nuclear wave packets in both electronic states move with different velocities, the oscillations of the electron momentum are damped. Assuming that only the first two states participate in the dynamics, the wave function can be expanded as:

$$\psi(x,R,t) = \chi_0(R,t)\phi_0(x;R) + \chi_1(R,t)\phi_1(x;R), \quad (15)$$

and the electronic momentum expectation value takes the form:

$$\langle p_x(t) \rangle = \int dR \chi_0^*(R,t)\chi_1^*(R,t) \int dx \phi_0(x;R) p_x \phi_1(x;R) + \text{c.c.} \quad (16)$$

Here, we considered the fact that the expectation value in a single state vanishes. The latter expression shows that indeed the fast oscillations in $\langle p_x(t) \rangle$ stem from the different phases of the wave packets in the two electronic states. It is obvious that $\langle p_x(t) \rangle$ is only non-zero if the nuclear wave packets in the two states have a spatial overlap which can be measured by the nuclear correlation function

$$c_{nm}(t) = |\langle \chi_n(t) | \chi_m(t) \rangle|, \quad (17)$$

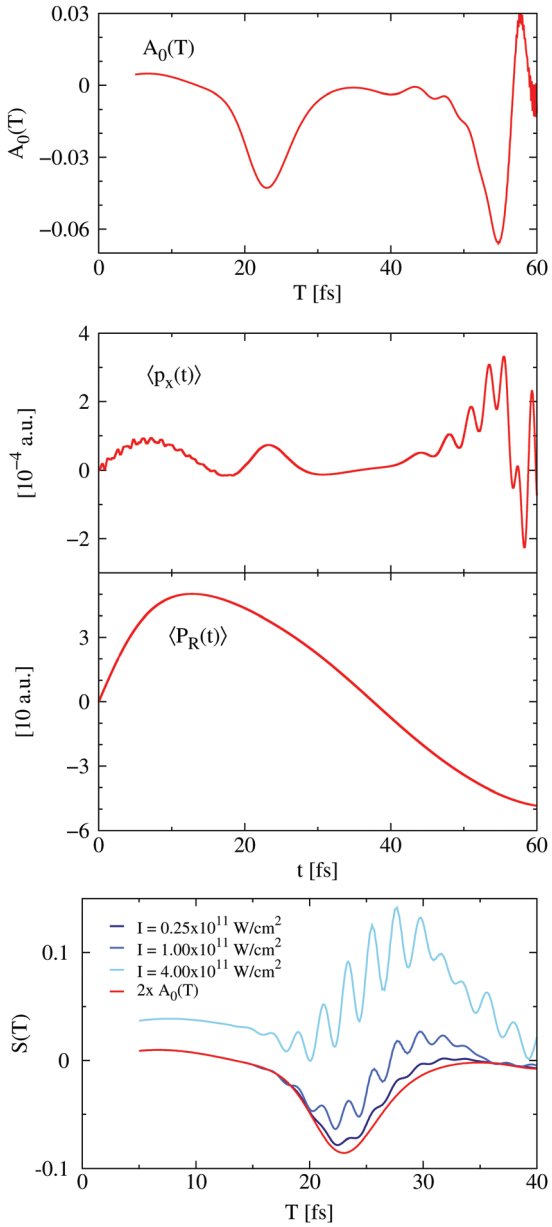

Fig. 6 Non-adiabatic dynamics. Upper panel: Time-resolved (integrated) asymmetry $A_0(T)$ probed with a λ_{XUV} = 60 nm (20.7 eV), 2.3 fs FWHM XUV pulse. Middle panels: Expectation values of the electron ($\langle p_x(t)\rangle$) and nucleus ($\langle P_R(t)\rangle$) momenta, as indicated. Lower panel: Sum of asymmetries $S(T)$ of the system interacting with an IR field with different intensities, as labeled. For comparison, twice the asymmetry $A_0(T)$ is included.

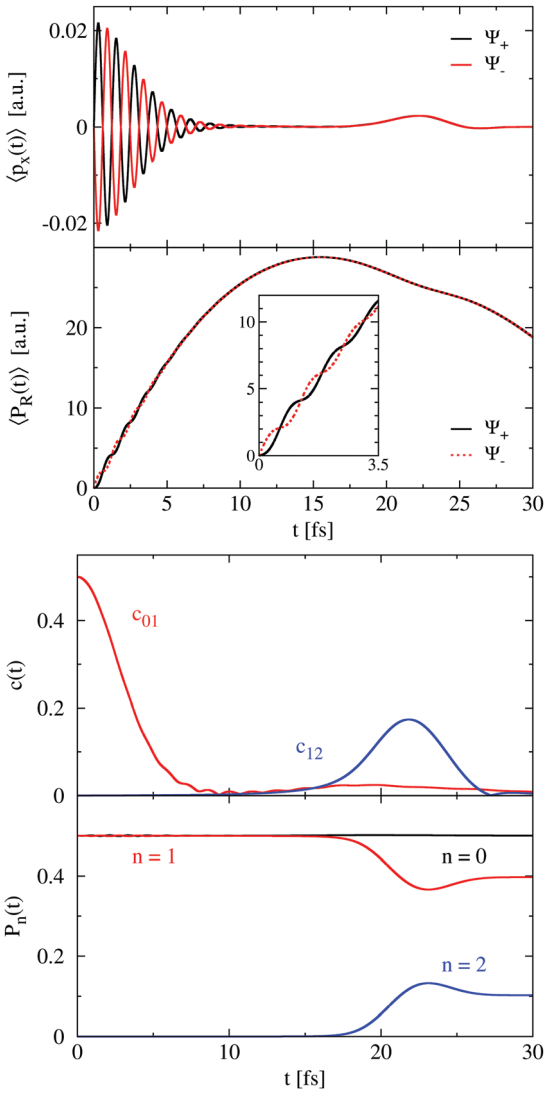

Fig. 7 Adiabatic dynamics in a superposition state: Upper panels: $\langle p_x(t)\rangle$ and $\langle P_R(t)\rangle$ for $\psi_+(t)$ (black) and $\psi_-(t)$ (red). Lower panels: Nuclear density $\rho(R,t)$, nuclear correlation function $c_{01}(t)$, $c_{12}(t)$, and population of the lowest electronic states $P_n(t)$.

where, $n = 0$ and $m = 1$. The function $c_{01}(t)$ is displayed in Fig. 7 and its decay explains the damping of the electron momenta in less than 10 fs. At later times, between 20 and 25 fs, the $\langle p_x(t)\rangle$ for both superposition states increases again to small positive values, however, without oscillations. This increase of $\langle p_x(t)\rangle$ is caused by a non-adiabatic transition to the second excited state, as can be realized with regard to the populations $P_n(t)$

$$P_n(t) = |\langle \varphi_n | \psi_\pm(t)\rangle|^2, \qquad (18)$$

and the nuclear correlation function $c_{12}(t)$, both displayed in Fig. 7. As can be seen, about 10% of the population of state $|\phi_1\rangle$ is transferred to $|\varphi_2\rangle$.

We note that the electronic coherences are also present in the asymmetry A_0 displayed in Fig. 2. There, they have a smaller amplitude because the interference term eqn (16) is smaller.

In order to resolve the fast oscillations, the ionizing XUV pulse has to be short enough in the time domain, or spectrally sufficiently broad to probe states $|\varphi_0\rangle$ and $|\varphi_1\rangle$. In Fig. 8, a comparison of the extracted asymmetries for several pulse lengths is shown. For the longest pulse with a (Gaussian) pulse width of 2.32 fs, the asymmetry describing the fast oscillations of $\langle p_x(t)\rangle$ in the first 10 fs is about 0.001. For shorter pulses, the absolute values of the asymmetry following the oscillations increase strongly. This can be understood as the asymmetry directly reflects $\langle p_x(t)\rangle$ – with increasing pulse length the average

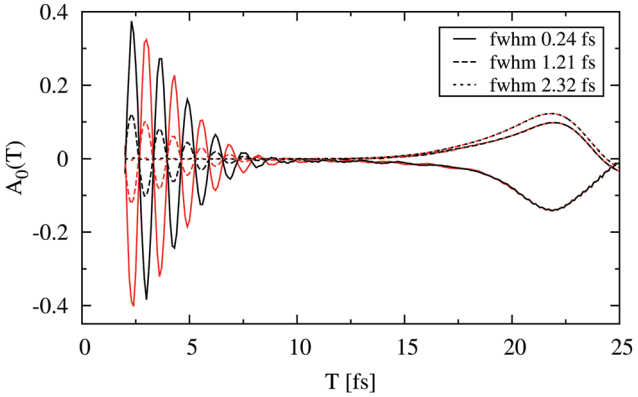

Fig. 8 Asymmetry of the adiabatic dynamics in a superposition state for $\psi_+(t)$ (black) and $\psi_-(t)$ (red) at different XUV pulse lengths, as labeled.

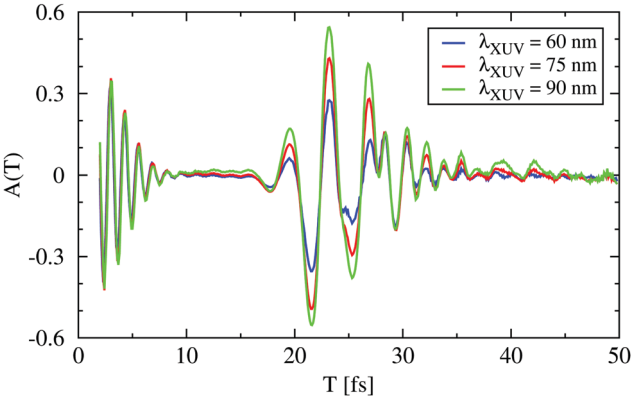

Fig. 9 Asymmetry of the adiabatic dynamics in the $\psi_+(t)$ superposition state, driven by a weak, few-cycle IR field centered around T_{IR} = 24 fs at different XUV wavelengths, as labeled.

over the oscillations being present in $\langle p_x(t)\rangle$ leads to an increase in the amplitude. From another perspective, the asymmetry in the PAD can be understood to originate from the interference of ionization pathways from two different electronic states.[22] Thus, the larger the spectral overlap, the more pronounced the asymmetry can be. It is apparent that the sign of the asymmetry is directly related to the sign of the electron momentum and thus to the phase of the bound electronic (and vibrational) wave packet.

The non-adiabatic transition at later times (around 20–25 fs) is probed by the asymmetry. However, here the asymmetry displays a different behavior: for the longest pulse (2.32 fs, corresponding to a spectral width of 0.78 eV), $A_0(T)$ is relatively large and positive, for shorter pulses (1.21 fs, corresponding to a spectral width of 1.50 eV) the asymmetry is reduced, and for the shortest pulse (0.24 fs, corresponding to a spectral width of 7.58 eV) even the sign of the asymmetry is changed. Please note, that the sign of the asymmetry (as well as the electron momentum $\langle p_x(t)\rangle$) is the same for both superposition states. The reason for this behavior is that only the shortest pulse is spectrally sufficiently broad to coherently probe all three populated electronic states $|\varphi_{0,1,2}\rangle$ with energetically overlapping photoelectron momentum distributions.

In order to further examine the role of the XUV spectral bandwidth in the asymmetry, we present results obtained upon ionization with different central wavelengths λ_{XUV} = 60, 75, and 90 nm (corresponding to photon energies of 20.66, 16.53, and 13.78 eV), while keeping the pulse length (and thus the spectral bandwidth) the same (0.24 fs FWHM, 7.58 eV). Additionally, a weak, few-cycle IR field interacts with the system, centered around T_{IR} = 24 fs. The resulting asymmetries $A(T)$ are shown in Fig. 9. As can be seen, the overall characteristics of $A(T)$ are the same for all three wavelengths, however, the absolute values of the asymmetry differ: the shorter the XUV wavelength, the smaller the absolute value of the asymmetry. Differently speaking, the closer the λ_{XUV} to the ionization threshold, the larger the measured asymmetry $A(T)$; for λ_{XUV} = 90 nm, asymmetry values as high as ±0.5 can be reached. The reason is that, as discussed above, the magnitude of the asymmetry in the PAD is related to the spectral overlap of the individual ionization pathways. Thus, the larger this overlap the more pronounced the asymmetry can be. In the limit of 100% spectral overlap, the asymmetry may reach values around $A = \pm 1$. For longer λ_{XUV} (and thus the closer to the ionization threshold), larger parts of the spectral bandwidth of the XUV pulse do not ionize the system. Thus, the absolute value of the spectral overlap decreases, while the relative value of overlaps increases, and with it the asymmetry.

4 Summary

We have investigated the possibility to spectrally observe the coupled electron–nuclear dynamics in a charge-transfer model system driven by moderately intense IR laser fields. We have shown that not only the electron dynamics induced by an IR field but also the intrinsic electron dynamics can be monitored *via* the asymmetry of the integrated photoelectron spectra. We can evoke a classical, intuitive picture, that upon ionization with an XUV pulse at time T, the electron retains its mean momentum and is emitted preferentially in the corresponding direction, leading to an asymmetry $A(T)$ in the photoelectron distribution. Here, stronger fields induce higher electron momenta which manifest themselves in larger absolute values of the asymmetry. Thereby, the energy-resolved photoelectron spectra and their asymmetries provide additional information on the systems dynamics: at times t, when the electron is driven to one side, the part of the electron wave packet moving to this side receives an additional boost, thus ending up at higher kinetic energies, while the part of the electron wave packet moving to the opposite side is decelerated, with the spectrum being shifted to lower kinetic energies. This leads to a pronounced energy-resolved asymmetry with opposite signs for higher and lower kinetic energies. Additionally, if the electron is strongly driven to one side at times when a non-adiabatic transition takes place, the photoelectron spectra (and the asymmetry) map these dynamics.

In order to separate the contributions of field-driven and intrinsic dynamics, we have investigated a new measure, namely the sum of asymmetries originating from two different

experiments with the carrier–envelope phases of the IR fields shifted by π. The sum thereby is a direct measure of the intrinsic dynamics, as long as the IR field strength is not too large to further induce non-transient population transfer. This relation can be applied to both, adiabatic and non-adiabatic dynamics in the presence of a moderately intense IR field.

As the sign of the asymmetry directly reflects the electron momentum expectation value, this suggests that the asymmetry is sensitive to the details of the momentum distribution of the electronic wave packet. We have confirmed this considering superposition states, where dynamics involving electronic coherences can be observed. If the XUV pulses are sufficiently short (spectrally broad) to coherently probe the coupled states, the asymmetry maps the phase relations present in the vibronic wave packet and also the non-adiabatic dynamics.

To conclude, time-resolved photoelectron spectroscopy and the asymmetries in the photoelectron momentum distribution are highly versatile tools to monitor intrinsic and field-driven electron dynamics and transient population transfer, allowing at the same time the adiabatic and non-adiabatic dynamics to be distinguished. This may help in examining various mixed dynamics in field-driven systems, *e.g.* proceeding in light-induced conical intersections, or multi-dimensional and multi-electron systems. Work along these lines is in progress.

Acknowledgements

The authors acknowledge the COST action XLIC. M. F. and V. E. thank the DFG for support within the FOR 1809. F. G. F. and S. G. highly acknowledge support from the German Science Foundation DFG, IRTG 2101.

References

1 A. Baltuška, T. Udem, M. Uiberacker, M. Hentschel, E. Goulielmakis, C. Gohle, R. Holzwarth, V. S. Yakovlev, A. Scrinzi, T. W. Hänsch and F. Krausz, *Nature*, 2003, **421**, 611–615.
2 J. Itatani, F. Quéré, G. L. Yudin, M. Y. Ivanov, F. Krausz and P. B. Corkum, *Phys. Rev. Lett.*, 2002, **88**, 173903.
3 M. Kitzler, N. Milosevic, A. Scrinzi, F. Krausz and T. Brabec, *Phys. Rev. Lett.*, 2002, **88**, 173904.
4 E. Goulielmakis, M. Uiberacker, R. Kienberger, A. Baltuska, V. Yakovlev, A. Scrinzi, T. Westerwalbesloh, U. Kleineberg, U. Heinzmann, M. Drescher and F. Krausz, *Science*, 2004, **305**, 1267–1269.
5 F. Krausz and M. I. Stockman, *Nat. Photonics*, 2014, **8**, 205–213.
6 M. Hentschel, R. Kienberger, C. Spielmann, G. A. Reider, N. Milosevic, T. Brabec, P. Corkum, U. Heinzmann, M. Drescher and F. Krausz, *Nature*, 2001, **414**, 509–513.
7 R. Kienberger, M. Hentschel, M. Uiberacker, C. Spielmann, M. Kitzler, A. Scrinzi, M. Wieland, T. Westerwalbesloh, U. Kleineberg, U. Heinzmann, M. Drescher and F. Krausz, *Science*, 2002, **297**, 1144.
8 T. Brabec and F. Krausz, *Rev. Mod. Phys.*, 2000, **72**, 545–591.
9 W. Domcke and G. Stock, *Acc. Chem. Res.*, 1997, **100**, 1–169.
10 M. Falge, V. Engel and S. Gräfe, *J. Phys. Chem. Lett.*, 2012, **3**, 2617–2620.
11 J. A. Davies, R. E. Continetti, D. W. Chandler and C. C. Hayden, *Phys. Rev. Lett.*, 2000, **84**, 5983–5986.
12 A. Stolow, A. E. Bragg and D. M. Neumark, *Chem. Rev.*, 2004, **104**, 1719–1758.
13 T. Suzuki, *Annu. Rev. Phys. Chem.*, 2006, **57**, 555–592.
14 S. A. Aseyev, Y. Ni, L. J. Frasinski, H. G. Muller and M. J. J. Vrakking, *Phys. Rev. Lett.*, 2003, **91**, 223902.
15 T. Pfeifer, M. J. Abel, P. M. Nagel, A. Jullien, Z.-H. Loh, M. J. Bell, D. M. Neumark and S. R. Leone, *Chem. Phys. Lett.*, 2008, **463**, 11–24.
16 M. F. Kling, C. Siedschlag, A. J. Verhoef, J. I. Khan, M. Schultze, T. Uphues, Y. Ni, M. Uiberacker, M. Drescher, F. Krausz and M. J. J. Vrakking, *Science*, 2006, **312**, 246.
17 P. Hockett, C. Z. Bisgaard, O. J. Clarkin and A. Stolow, *Nat. Phys.*, 2011, **7**, 612–615.
18 T. Seideman, *Phys. Rev. A: At., Mol., Opt. Phys.*, 2001, **64**, 042504.
19 T. Seideman, *Annu. Rev. Phys. Chem.*, 2002, **53**, 41–65.
20 G. L. Yudin, A. D. Bandrauk and P. B. Corkum, *Phys. Rev. Lett.*, 2006, **96**, 063002.
21 O. Smirnova, M. Spanner and M. Y. Ivanov, *J. Phys. B: At., Mol. Opt. Phys.*, 2006, **39**, S307.
22 S. Gräfe, V. Engel and M. Y. Ivanov, *Phys. Rev. Lett.*, 2008, **101**, 103001.
23 S. Shin and H. Metiu, *J. Chem. Phys.*, 1995, **102**, 9285–9295.
24 S. Shin and H. Metiu, *J. Phys. Chem.*, 1996, **100**, 7867–7872.
25 M. Erdmann, P. Marquetand and V. Engel, *J. Chem. Phys.*, 2003, **119**, 672–679.
26 M. Erdmann and V. Engel, *J. Chem. Phys.*, 2004, **120**, 158–164.
27 M. Erdmann, S. Baumann, S. Gräfe and V. Engel, *Eur. Phys. J. D*, 2004, **30**, 327–333.
28 S. Gräfe and V. Engel, *Chem. Phys.*, 2006, **329**, 118–125.
29 M. Falge, V. Engel and S. Gräfe, *J. Chem. Phys.*, 2011, **134**, 184307.
30 A. Abedi, F. Agostini, Y. Suzuki and E. K. U. Gross, *Phys. Rev. Lett.*, 2013, **110**, 263001.
31 M. Falge, P. Vindel-Zandbergen, V. Engel, M. Lein, B. Y. Chang and I. R. Sola, *J. Phys. B: At. Mol. Phys.*, 2014, **47**, 124027.
32 F. Agostini, A. Abedi, Y. Suzuki, S. Min, N. T. Maitra and E. Gross, *J. Chem. Phys.*, 2015, **142**, 084303.
33 J. Albert, D. Kaiser and V. Engel, *J. Chem. Phys.*, 2016, **144**, 171103.
34 K. Hader, J. Albert, E. Gross and V. Engel, *J. Chem. Phys.*, 2017, **146**, 074304.
35 M. D. Feit, J. A. Fleck and A. Steiger, *J. Comput. Phys.*, 1982, **47**, 412–433.
36 S. G. J. M. Frigo, *ICASSP conference proceedings*, 1998, **3**, p. 1381.
37 R. Kosloff and H. Tal-Ezer, *Chem. Phys. Lett.*, 1986, **127**, 223–230.
38 R. Heather and H. Metiu, *J. Chem. Phys.*, 1987, **86**, 5009.
39 A. Keller, *Phys. Rev. A: At., Mol., Opt. Phys.*, 1995, **52**, 1450.

